Aerospace Science and Technology 152 (2024) 109307

Contents lists available at ScienceDirect

Aerospace Science and Technology

journal homepage: www.elsevier.com/locate/aescte

Adaptive track approach for multiple sources scenarios during radar survey for space surveillance applications

M.F. Montaruli [a,*], P. Di Lizia [a], S. Tebaldini [b], G. Bianchi [c]

[a] Department of Aerospace Science and Technology, Politecnico di Milano, Via G. La Masa 34, 20156, Milan, Italy
[b] Department of Electronics, Information and Bio-engineering, Politecnico di Milano, Via Ponzio 34/5 20133, Milan, Italy
[c] Istituto di Radioastronomia, Istituto Nazionale di Astrofisica, Via P. Gobetti 101, 40129, Bologna, Italy

ARTICLE INFO

Communicated by Christian Circi

Keywords:
Space surveillance and tracking
Space debris
MUSIC
Radar array
Proximity operations
Fragmentations

ABSTRACT

The increasing population of resident space objects is currently fostering many space surveillance initiatives, which rely on the use of on-ground sensors. In particular, survey radars allow to first characterise the target orbit from a single transit, through measurements which are Doppler shift, slant range and angular profile. In this framework, the Music Approach for Track Estimate and Refinement (MATER) algorithm was developed to compute the angular track through the MUltiple SIgnal Classification (MUSIC), by solving possible ambiguities which may arise because of the receiver array geometry.

This work presents the MATER extension to the case in which multiple sources are simultaneously detected by the sensor. For each detected source, the signal Direction of Arrival (DOA) is computed through MUSIC, and, if no prediction is exploited, possible ambiguous solutions arise. The computation is repeated for the entire observation, and all the estimations related to a specific target are grouped based on the angular sequence shape and the detection epochs. Finally, the possible ambiguity problem is solved, and the angular profile is obtained through a quadratic regression in time.

The algorithm is numerically tested on a survey observation simulation. The detection length depends on the impinging signal intensity, and the angular accuracy is in the order of 1e-03 deg. A sensitivity analysis highlights that a transmitted power decrease shortens the detection length, with no remarkable angular accuracy deterioration. An additional simulation shows that in proximity operation monitoring MATER performance depends on the mutual geometry between target and chaser, as it may bring down the reciprocal angular distance under the resolution level. Nevertheless, it is always possible to identify the presence of both sources through the eigenvalues analysis of the signal correlation matrix. Finally, the simulation of a fragments cloud observation highlights that MATER performance depends both on the size of the observed fragment, as this is strictly linked to the signal detected by the receiver, and on the simultaneous detection of other fragments with a more effective signal.

1. Introduction

In the last decades the space pollution has become of utmost importance for space agencies and institutions all around the world [1]. Space Surveillance and Tracking (SST) framework is in charge of monitoring in orbit traffic, providing services such as Collision Avoidance [2] [3], Re-entry [4] and Fragmentations [5]. Besides this, also manoeuvre detection [6] and proximity operations [7] [8] [9] play a key role in space traffic management activities. In this context, on ground-based sensors are mostly used to maintain satellites catalogue, and they can be distinguished in laser, optical and radar [10]. Among them, survey means are fundamental, as they can acquire the measurements of an observed target with no transit prediction, that is even when it is not catalogued. In particular, survey radars allow to fully characterise the target orbit from a single transit, through an Initial Orbit Determination (IOD) process based on the acquired measurements, which are slant range (SR), Doppler shift (DS) and angular profile. The latter measurement is usually obtained by a static beamforming approach (as in [11] [12] and [13]) which generates one or more electronic beams of constant shape. These beams can be held fixed or steered differently in time to scan the

* Corresponding author.
E-mail address: marcofelice.montaruli@polimi.it (M.F. Montaruli).

https://doi.org/10.1016/j.ast.2024.109307
Received 4 October 2023; Received in revised form 20 May 2024; Accepted 10 June 2024
Available online 12 June 2024

sensor field of view (FoV). With this strategy, both angular accuracy and resolution are limited by the beam width, negatively affecting the accuracy of the IOD result.

To improve the angular track accuracy, multireceivers radars devoted to space surveillance can take advantage of interferometric techniques. In fact, the signal Direction of Arrival (DOA) in the receiver FoV can be estimated by fusing the data collected by the array elements, calculating the signal correlation matrix (CM) and then analysing it using an adaptive beamforming technique. By this strategy, the array pattern automatically adapts to the incoming signal without the need to generate static beams a-priori. It should be noted that with this approach the data stream may be too large to be processed in real time, so it is essential to record raw data and process them offline. In this framework, [14] presents the Music Approach for Track Estimate and Refinement (MATER) algorithm, which is devoted to reconstruct the angular track of a single source detected. It exploits MUSIC [15] to estimate the signal DOA, and solves the ambiguous estimations, occurring because of the mutual distance among the array elements, through either geometrical or statistical considerations. The resulting angular track accuracy is in the order of 1e-03 deg. Then, [16] also considers the effects of the signal integration time, during which the source moves in the receiver FoV, partially deteriorating the angular track accuracy. Moreover, [16] introduces an alternative way to solve the ambiguity in MATER, through an approach, at a signal processing level, addressed as *delta-k* technique.

As mentioned above, MATER algorithm was developed to process data collected from a single source observation. However, in SST-related operations, multiple targets can be detected simultaneously by a survey radar. With the static beamforming strategies typically employed, this is only possible if multiple beams scan different regions of the receiver FoV simultaneously. In any case, these approaches prevent from distinguishing targets which are so mutually close to be visible by the same beam, like during monitoring a fragments cloud or close proximity operations. On the contrary, MATER algorithm provides a higher angular accuracy and resolution compared to the static beamforming approaches, and this would allow to better distinguish among different sources simultaneously detected. For this reason, the purpose of this work is to extend MATER algorithm to manage multiple sources scenarios.

After having recalled the signal DOA estimation problem in Sec. 2 and the *delta-k* technique to solve the ambiguous solutions in Sec. 3, Sec. 4 presents the resulting algorithm, which is then numerically tested for survey operations in Sec. 5. It is worth to point out that the targets detected in such situations generally feature remarkably different relative velocities with respect to the sensor stations and, so, different Doppler shift effects of the transmitted signal. Thus, a proper channelisation strategy would allow to process only the signal reflected from a specific target, reducing the problem to a single source scenario. This is not the case during a proximity operation monitoring and a fragments cloud observation, in which the measured Doppler shift of the detected targets are similar, as they have a similar relative motion with respect to the ground stations. For this reason, these scenarios are discussed in Sec. 6 and Sec. 7.

2. Signal direction of arrival estimation

As mentioned in Sec. 1, the signal CMs can be created from the signal acquired by a radar array through interferometry, and later processed to estimate the signal DOA. In MATER, this operation is performed through MUSIC algorithm [15], which allows to estimate the DOAs for multiple signals detected simultaneously, and this is a key aspect to reconstruct the angular track of multiple satellites simultaneously observed, which is the objective of this work. Both data model and MUSIC algorithm detail descriptions can be found in [14] and in [16], and are briefly recapped as follows.

Let's consider the signal received by the array at any time instant:

$$\boldsymbol{x}(t) = \boldsymbol{a}(\Delta\boldsymbol{\gamma})\, s(t) + \boldsymbol{n} \tag{1}$$

where $\boldsymbol{a}(\Delta\boldsymbol{\gamma})$, $\boldsymbol{n}$ and $s(t)$ indicate the steering vector, the noise, and the envelop of the signal impinging on the array, respectively. In particular, $\Delta\boldsymbol{\gamma} = \left[\Delta\gamma_1\,,\, \Delta\gamma_2\right]^T$ represents the two angular deviations of the detected signal, in azimuth and elevation respectively, relative to the line of sight, hence denoting the signal DOA in the sensor reference frame.

If N_s sources are simultaneously detected, Eq. (1) can be generalised as:

$$\boldsymbol{x}(t) = \sum_{z=1}^{N_s} \boldsymbol{a}(\Delta\boldsymbol{\gamma}_z)\, s_z(t) + \boldsymbol{n} \tag{2}$$

Based on $\boldsymbol{x}(t)$, the signal Covariance Matrix (CM) can be computed as:

$$\boldsymbol{R}_{\boldsymbol{xx}} = E\left[\boldsymbol{x}(t)\boldsymbol{x}(t)^H\right] \tag{3}$$

where $E[\cdot]$ is the expected value operator and $\boldsymbol{x}(t)^H$ is the hermitian of $\boldsymbol{x}(t)$.

In the discrete time domain, N_k is considered as the number of signal samplings which are integrated to provide a single CM. For the k-th snapshot, $\boldsymbol{a}(\Delta\boldsymbol{\gamma})$, $s(t)$ and $\boldsymbol{n}$ can be written as $\boldsymbol{a}(\Delta\boldsymbol{\gamma})_k$, s_k and $\boldsymbol{n}_k$ respectively, and Eq. (1) becomes:

$$\boldsymbol{x}_k = \boldsymbol{a}(\Delta\boldsymbol{\gamma})_k\, s_k + \boldsymbol{n}_k \tag{4}$$

Thus, the discrete CM resulting from the integration can be expressed as:

$$\hat{\boldsymbol{R}}_{\boldsymbol{xx}} = \frac{1}{N_k}\sum_{k=1}^{N_k} \boldsymbol{x}_k \boldsymbol{x}_k^H \tag{5}$$

MUSIC algorithm searches for the signal DOA by splitting the $\boldsymbol{R}_{\boldsymbol{xx}}$ space in signal and noise subspaces, which are assumed to be orthogonal (based on the assumption that signal and noise are uncorrelated). By denoting the largest N_s eigenvalues matrix as $\boldsymbol{\Lambda}_{\boldsymbol{s}}$ and the corresponding eigenvectors subspace as $\boldsymbol{U}_{\boldsymbol{s}}$ and, similarly, by indicating noise subspace matrices as $\boldsymbol{\Lambda}_{\boldsymbol{n}}$ and $\boldsymbol{U}_{\boldsymbol{n}}$, the CM can be decomposed as:

$$\boldsymbol{R}_{\boldsymbol{xx}} = \boldsymbol{U}_{\boldsymbol{s}}\boldsymbol{\Lambda}_{\boldsymbol{s}}\boldsymbol{U}_{\boldsymbol{s}}^H + \boldsymbol{U}_{\boldsymbol{n}}\boldsymbol{\Lambda}_{\boldsymbol{n}}\boldsymbol{U}_{\boldsymbol{n}}^H \tag{6}$$

Based on this, MUSIC estimates the quantity $\boldsymbol{\Delta\gamma}$ through the maximisation of the following spectrum, which represents the array response to the impinging wave:

$$P(\Delta\boldsymbol{\gamma}) = \boldsymbol{a}(\Delta\boldsymbol{\gamma})^H \boldsymbol{U}_{\boldsymbol{s}}\boldsymbol{U}_{\boldsymbol{s}}^H \boldsymbol{a}(\Delta\boldsymbol{\gamma}) \tag{7}$$

By considering that $\boldsymbol{U}_{\boldsymbol{n}}^H \boldsymbol{a}(\boldsymbol{\Delta\gamma}) = 0$, due to the orthogonality between signal and noise subspaces, the estimate $\boldsymbol{\Delta\gamma}$ can be computed alternatively through the maximisation of the following spectrum:

$$P(\boldsymbol{\Delta\gamma}) = \frac{1}{\boldsymbol{a}(\boldsymbol{\Delta\gamma})^H \boldsymbol{U}_{\boldsymbol{n}}\boldsymbol{U}_{\boldsymbol{n}}^H \boldsymbol{a}(\boldsymbol{\Delta\gamma})} \tag{8}$$

Then, since $\boldsymbol{U}_{\boldsymbol{n}}\boldsymbol{U}_{\boldsymbol{n}}^H = \boldsymbol{I} - \boldsymbol{U}_{\boldsymbol{s}}\boldsymbol{U}_{\boldsymbol{s}}^H$ (where $\boldsymbol{I}$ is a $M \times M$ identity matrix), an alternative formulation can be derived:

$$P(\boldsymbol{\Delta\gamma}) = \frac{1}{\boldsymbol{a}(\boldsymbol{\Delta\gamma})^H \left[\boldsymbol{I} - \boldsymbol{U}_{\boldsymbol{s}}\boldsymbol{U}_{\boldsymbol{s}}^H\right] \boldsymbol{a}(\boldsymbol{\Delta\gamma})} \tag{9}$$

To obtain a unique solution of Eq. (9), the spacing between samples of the signal, which is provided by the array elements position, must be lower than the half-wavelength [17]. As a consequence, if the spacing is longer than that, spatial ambiguity (aliasing) occurs and so grating lobes appear. As discussed in [14] and [16], their angular span from the correct DOA estimate can be a-priori predicted as:

$$\Delta\theta_x \approx \arcsin\frac{i\,\lambda}{d_x}$$

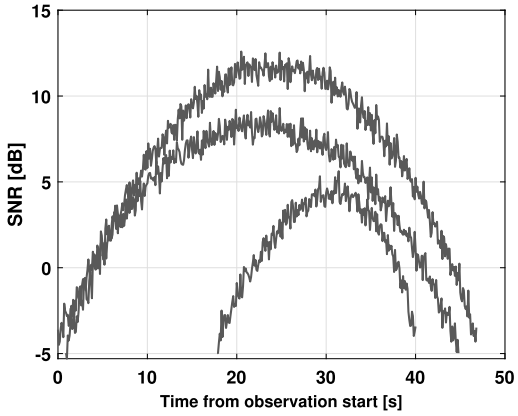

Fig. 1. MATER for multiple sources scenario: generic SNR profile acquired during a survey observation. It is possible to appreciate the presence of multiple detected signals, that is multiple observed sources, at the same epochs.

$$\Delta\theta_y = \arcsin \frac{j\,\lambda}{d_y} \tag{10}$$

Given this problem, ad-hoc solutions shall be identified for the DOA estimation ambiguities. This is the purpose of MATER algorithm [14], and the present work discusses its extension to the multiple sources scenario, that is when $N_s > 1$, by solving the ambiguity problem through the *delta-k* method.

3. Delta-k technique for signal DOA estimation in multireceiver radars

From Eq. (10) it is evident that signals at different frequencies feature different angular shifts of the ambiguous DOA estimations with respect to the correct solution. Based on this consideration, [16] presents the *delta-k* technique application to multireceivers radars.

Let's generalise Eq. (10) for any coordinate as:

$$\Delta\theta = \arcsin \frac{m\,c}{d\,f} \tag{11}$$

where d is the generic physical distance among array elements, m the generalisation of i and j indexes, and c is the speed of light. From Eq. (11) it is clear that two unmodulated continuous waves frequencies f_1 and f_2, reflected by a same source, would feature different angular shifts $\Delta\theta_1$ and $\Delta\theta_2$ of the m-th ambiguity with respect to the correct DOA. Thus, the correct solution can be identified if the difference $|\Delta\theta_2 - \Delta\theta_1|$ is larger than the sensor angular accuracy $\Delta\theta_n$, that is:

$$\left|\arcsin\left(\frac{m\,c}{d\,f_2}\right) - \arcsin\left(\frac{m\,c}{d\,f_1}\right)\right| > \Delta\theta_n \tag{12}$$

4. MATER extension to the multiple sources scenario

During survey observations, multiple sources can be simultaneously detected. This can occur also during the observation of a formation flying, a fragments cloud, or a proximity operation. In these scenarios, the detection epochs of the target signals overlap, as represented in Fig. 1, which reports the simulated SNR (Signal to Noise Ratio) trend during a generic survey observation, and where it is possible to appreciate the simultaneous presence of the signals from multiple sources at the same epochs.

In these scenarios, MATER algorithm [14] can be extended to derive the tracks of targets whose detection epochs overlap, that is when, for some epochs, the number of observed sources N_s is larger than 1. In this case, at a generic observation epoch, multiple DOAs shall be estimated, one for each observed target, to which ambiguous solutions are added if no a-priori transit prediction is available.

To adapt MATER to the multiple sources scenario, a key point is to isolate the detection epochs related to a same target. In this work this operation is accomplished through the SNR profile, from which it is possible to derive the information about the number of detected targets N_s at a given epoch, that is the number of impinging signals that, at that epoch, overcome a SNR threshold, and this represents the number of DOAs N_s to search for. Given this pre-processing phase, the extension of MATER algorithm to the multiple sources scenario is described hereafter.

4.1. Catalogued objects

In case the observed objects are catalogued, that is reliable transit predictions of the targets are present, MATER derives the angular track as illustrated in Fig. 2. In the track estimate phase, the DOAs are estimated time by time from the CM eigen-decomposition, thanks to an optimisation process aimed at maximising Eq. (9). The reference tracks (derived from pass prediction) can directly be used as first guesses in the optimisation, such that the DOA corresponding to the closest peak is selected. In this way, for each observation epoch, one DOA estimation per reference track is computed. By this way, one single DOA sequence per observed object is obtained by grouping all the estimations related to a same reference track, as reported in Fig. 3a for the same observation as in Fig. 1.

Once the DOA estimate at each observation epoch has been computed, the algorithm proceeds to the track refinement phase, whose purpose is to derive the time evolution of the object angular coordinates in the sensor FoV during the pass. This goal is achieved by first identifying DOAs estimations related to a single observed object, according to the epochs of the transit prediction and of the recorded SNR profile. Then, outliers are removed and a quadratic regression in time is performed on the two angular coordinates separately, such that the time-dependent profiles $\Delta\gamma_1(t)$ and $\Delta\gamma_2(t)$ are obtained. The result is shown in Fig. 3b.

4.2. Uncatalogued objects

For the uncatalogued case (that is when the detected measurements do not correlate to any catalogued object) the DOA estimation ambiguity cannot be solved through transit prediction. In this case, track shall be reconstructed based on acquired measurements only, through the flow described in Fig. 4.

As Sec. 3 describes, two CMs, referred to the same source reflection but related to two different frequencies, feature the same correct DOA solution, but different ambiguous estimations, and to exploit this property Eq. (12) shall be satisfied.

The track estimate phase is performed on the two CM sequences separately (related to the two frequencies at which they are generated). From the detection block it is possible to identify the number of observed objects for each time instant, that is the number of DOA estimations to be reconstructed. So, for each observation epoch, the number of observed sources N_s is identified and the N_s eigenvectors $\boldsymbol{U}_s$ related to the largest N_s eigenvalues are taken into account. For each $\boldsymbol{U}_s$, both a coarse computation and a maximisation process is performed, as follows. First, the coarse computation (on a grid of angular coordinates) identifies the highest N_p peaks of the pattern obtained from Eq. (9). The peaks searching is performed by finding the global maximum first. Then, the other $N_p - 1$ peaks coordinates are determined analytically, according to the angular shift of Eq. (10). These N_p angular coordinates pairs represent the first guesses for the maximisation process of Eq. (9). This operation is repeated, at each observation epoch, for all the N_s detected sources. At the end, $N_p \times N_s$ angular positions in the receiver FoV are identified at each epoch. Fig. 5a represents the track estimate result for the uncatalogued case. It can be noticed that the receiver FoV is more populated of estimations than the one in Fig. 3a, as the am-

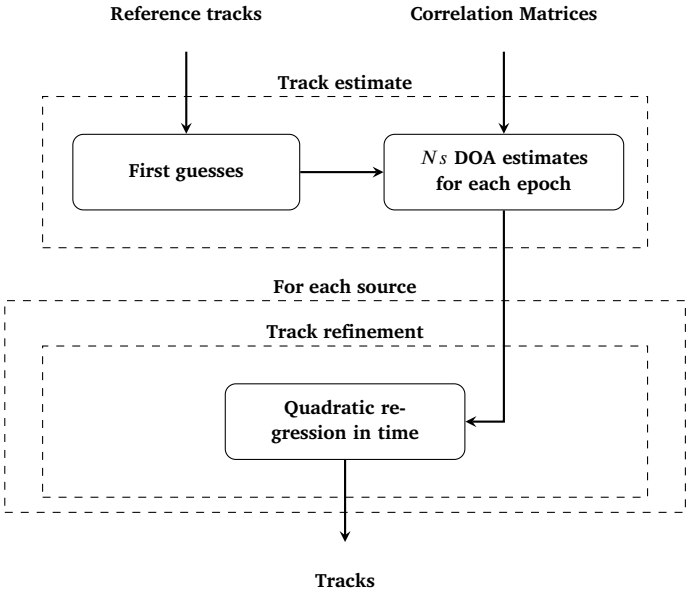

Fig. 2. MATER for the multiple sources scenario: catalogued case flowchart.

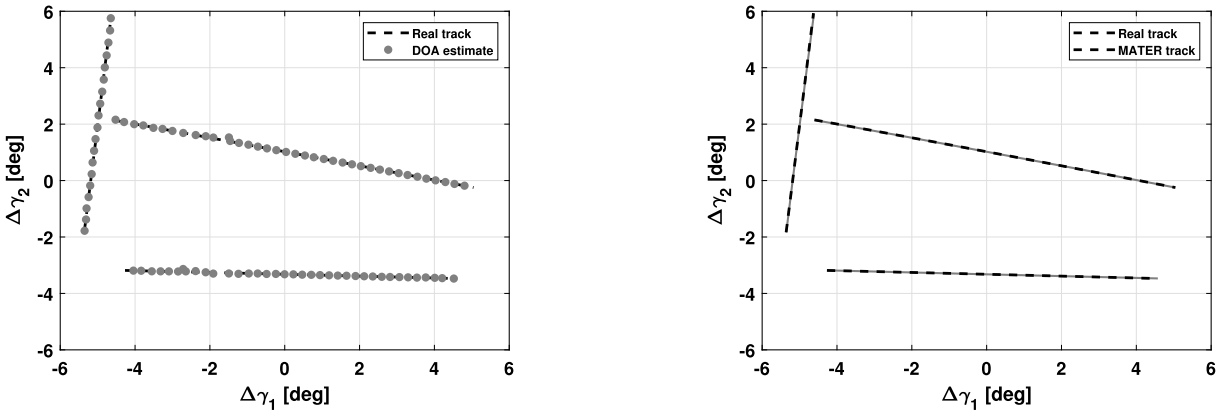

(a) Track estimate.

(b) Track refinement.

Fig. 3. MATER for multiple sources scenario: track estimate and refinement result for the catalogued case.

biguous estimations are represented as well. This process is repeated for both the CM sequences.

In the following track refinement phase the *delta-k* method is applied by retaining, for each observation epoch, just the N_s estimations featuring the minimum angular deviation among the DOAs computed from the two CMs. This results in a FoV with less DOAs estimations, as reported in Fig. 5b.

At this point, all the DOAs related to a same source are isolated based on the detection epochs. Next, the estimations are clustered according to a RANdom SAmple Consensus algorithm [18]. The clustering is conducted in the FoV, to correctly group the angular coordinates estimations, and the corresponding epoch is then associated. At this point, a quadratic regression in time, for the two angular coordinates separately, is performed. Finally, one track for each source is obtained, similarly to those reported in Fig. 3b.

5. Survey numerical analysis

A numerical analysis is here performed to assess MATER algorithm in survey applications, by taking the BIstatic RAdar for LEo Survey (BIRALES) as reference [19].

5.1. BIRALES

BIRALES is an Italian bistatic radar system contributing to the European Space Surveillance and Tracking (EUSST) sensor network [20]. Its transmitter is the TRF (Trasmettitore a Radio Frequenza, Radio Frequency Transmitter) located at the Italian Joint Test Range of Salto di Quirra in Sardinia, while the receiver is part of the Northern Cross radio telescope of the Radio Astronomical Station of Medicina (Bologna, Italy). Currently, a new transmitter is being developed and installed to grant a better intersection of the field of regard of the two stations [21].

The portion of the Northern Cross radio telescope dedicated to BIRALES receiver is an array composed of 8 cylindrical parabolic concentrators aligned towards the North-South direction [19]. Each cylinder contains four receivers installed on the focal line (aligned with the East-West direction). Therefore, the receiving system is composed of a matrix of 8x4 receivers spaced 5.67 m in East-West (d_{E-W}) and 10 m in North-South (d_{N-S}).

Doppler shift and slant range measurements are provided through a Continuous Wave (CW) and a CHIRP signal respectively. The CW is also exploited to derive the angular track, which is currently operationally

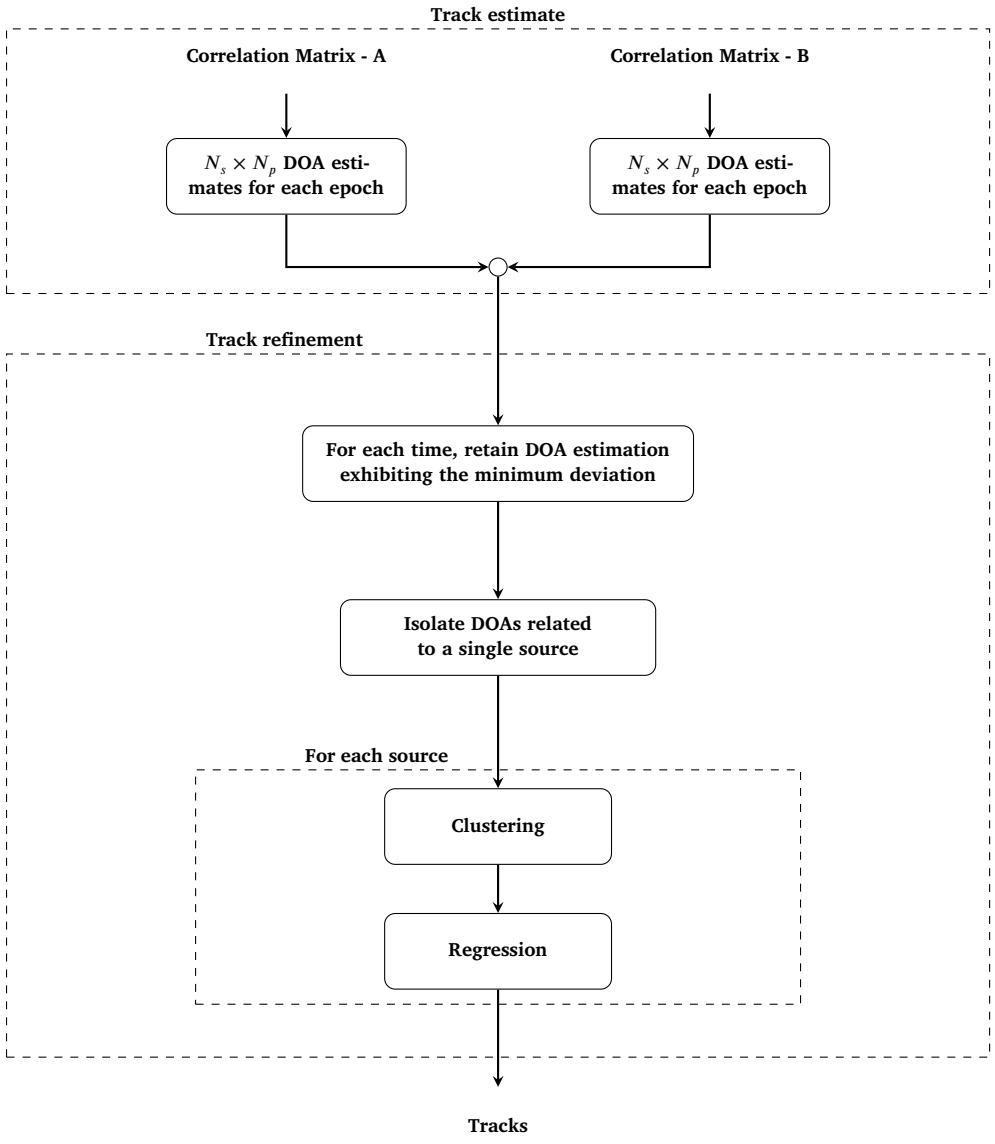

Fig. 4. MATER for the multiple sources scenario: uncatalogued case flowchart. The *delta-k* criterion is used to solve the ambiguity.

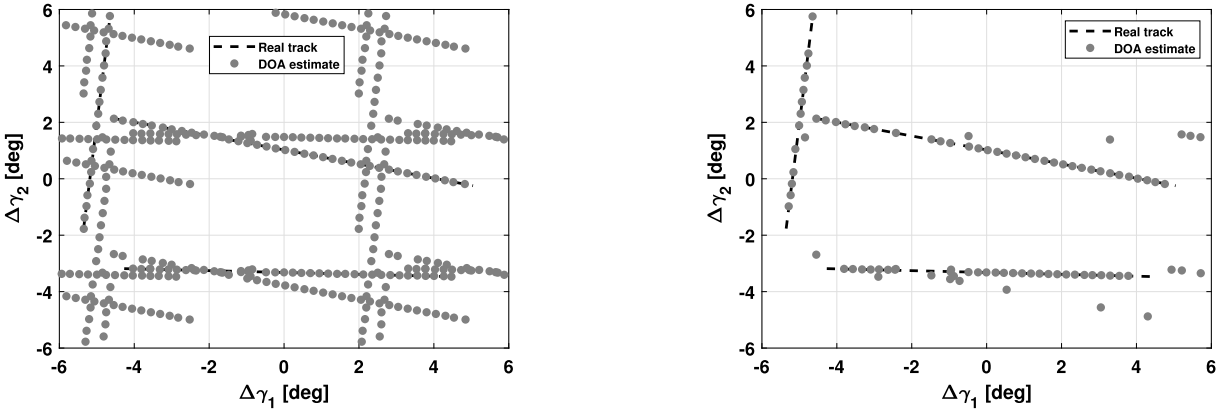

(a) Track estimate.

(b) *delta-k* technique DOA estimation selection.

Fig. 5. MATER for multiple sources scenario: track estimate result for the uncatalogued case.

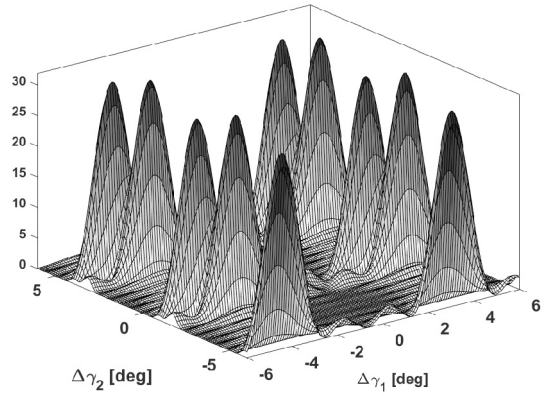

Fig. 6. BIRALES: array response based on MUSIC for 2 sources observation.

retrieved through a static beamforming approach [22]. However, BIRALES back-end is undergoing an upgrade process which will allow to exploit an adaptive beamforming technique.

Based on these characteristics and referring to Sec. 2, the number of array elements is $M = N_x \times N_y = 32$, being $N_x = 4$ and $N_y = 8$. Thus, $\boldsymbol{a}(\boldsymbol{\Delta\gamma})$ dimension is 32×1 and $\widehat{\boldsymbol{R}}_{\boldsymbol{xx}}$ size is 32×32, regardless the number of sampling N_k. It is worth to point out that BIRALES back-end allows to record raw data and this would allow MATER algorithm to be run in post-processing.

BIRALES does not meet the conditions stated in Sec. 2 to have a unique solution, being $\lambda = 0.73$ m, $d_x = 5.67$ m and $d_y = 10$ m. This yields an ambiguity in the array response to the impinging signal, and multiple peaks (i.e., multiple DOA solutions) are simultaneously present at any epoch, as represented in Fig. 6, which shows MUSIC output in function of $\Delta\gamma_1$ and $\Delta\gamma_2$ (defined in Sec. 2), for a $N_s = 2$ sources observation. Since the receiver pointing can be moved along the local meridian (that is in elevation only), $\Delta\gamma_1$ and $\Delta\gamma_2$ turn out to represent the East-West and North-South directions, respectively. The peaks lobes are larger along $\Delta\gamma_1$, as the East-West direction has less receivers than the North-South one (4 against 8), and this theoretically makes DOA estimation more accurate along the $\Delta\gamma_2$ direction. However, the estimation accuracy depends on the angular path length described by the source in the receiver FoV during the signal integration time of the acquisition [16].

5.2. Nominal analysis

A synthetic data set composed of 530 transits related to 253 LEO objects from the NORAD catalogue [23] is analysed. Table 1 shows the orbital characteristics distribution of these objects, in terms of quartiles on semi-major axis, eccentricity, inclination, right ascension of the ascending node, and argument of periapsis. The analysis considers an observation window of one day, on June 16th, 2021. These passes temporally superimpose each other, and they can be subdivided in slots, each slot being composed of a sequence of temporally overlapping transits (with overlapping SNR trends, like in Fig. 1). The correspondence between the number of overlapping transits and the slots is reported in Table 2: 129 slots composed of 2 temporally overlapping passes, 50 slots with 3 temporally overlapping passes, and so on. The transits projections in the measurements space provide their nominal angular track. The transmitter and receiver pointing angles, in terms of azimuth and elevation, are set equal to [7, 40.5] deg and [0, 60] deg respectively.

For the simulation, the two central frequencies involved in the *delta-k* technique for the multireceiver radars are set to 411.5 MHz and 413.5 MHz. From Eq. (12), this frequency choice induces an angular shift of the ambiguous estimations of 0.017 deg, which is assumed to be on average larger than the sensor angular accuracy.

Table 1
Survey nominal simulation: distribution of the target orbital characteristics, in terms of the three quartiles of semi-major axis (a), eccentricity (e), inclination (i), right ascension of the ascending node (Ω) and argument of periapsis (ω).

	a [km]	e	i [deg]	Ω [deg]	ω [deg]
25%	7463.9	2.7e-03	65.1	100.2	82.4
50%	7768.9	7.5e-03	74.1	187.5	154.2
75%	7875.4	2.5e-02	99.0	282.8	253.6

Table 2
Survey nominal simulation: slots composed of passes temporally overlapping each other.

N. of passes per slot	2	3	4	5	6	7	8	TOT
Obj. per slot	129	50	17	4	2	2	1	530

Then, for both of frequencies, the measured SNR is simulated as:

$$SNR = 10\log_{10}\left(\frac{P_{rx}}{k\,Bw\,T_{eq}}\right) \tag{13}$$

where $k = 1.380658$ e-23 is the Boltzmann's constant, T_{eq} is the equivalent temperature of the system (set to 86 K) and Bw is the channel bandwidth, corresponding to the frequency f_s used to sample the signal and set equal to 1 kHz. For a bistatic radar, the received power P_{rx} is modelled as:

$$P_{rx} = \frac{P_{tx}\,G_{tx}\,G_{rx}\,RCS\,c^2}{(4\pi)^3\,f_c^2\,\rho_{tx}^2\,\rho_{rx}^2} \tag{14}$$

where P_{tx} is the transmitted power (1e5 W is used as nominal value), G_{tx} and G_{rx} are the transmitter and receiver gain respectively (they depend on the angular position of the source in the transmitter and receiver FoV), RCS is the object Radar Cross Section and is set to 1 m^2, c is the light speed, f_c is the frequency considered (either 411.5 MHz or 413.5 MHz), ρ_{TX} and ρ_{RX} are the distances between the orbiting object and the transmitter and receiver, respectively. A Gaussian noise with a standard deviation of 0.5 dB is added to include the effect of the RCS fluctuation. To model the impinging signal, Eq. (4) is evaluated at each k-th snapshot, with $\boldsymbol{a}(\boldsymbol{\Delta\gamma})_k$ obtained considering the angular position of the source in the receiver FoV, s_k according to the SNR in Eq. (13) and the noise $\boldsymbol{n}_k$ through a Gaussian distribution with standard deviation equal to 1.

According to the 1 KHz f_s selected, one CM is created along the pass every 0.1 s (the integration time) with $N_k = 100$ snapshots, through the implementation of Eq. (5). The mean snapshot epoch is taken as the DOA estimation epoch. Thus, if the noise effect is neglected, the half integration time theoretically bounds the angular error in the DOA estimation, depending on the relative velocity between the station and the observed target. The angular error generated by the integration time resolution is then mediated by the clustering and the regression phases, where the outliers are rejected.

Starting from these data, MATER is run to assess its performance, and its accuracy is analysed in terms of the three quartiles (25%, 50% and 75%), on the entire data set, of the root mean square error (RMSE), computed as:

$$\eta = \sqrt{\frac{1}{N}\sum_i \left(\Delta\gamma_i - \overline{\Delta\gamma_i}\right)^2} \tag{15}$$

for the two angular coordinates separately. $\Delta\gamma_i$ and $\overline{\Delta\gamma_i}$ stand for the estimated and the correct angular position, respectively, at the i-th detection epoch, whose total number is N.

First, MATER is run by assuming that all the objects are catalogued, i.e. an a-priori estimate of their orbit is available. The results are summarised in Table 3, which reports the three RMSE quartiles for the two angular coordinates separately. The values range between 1e-03 and

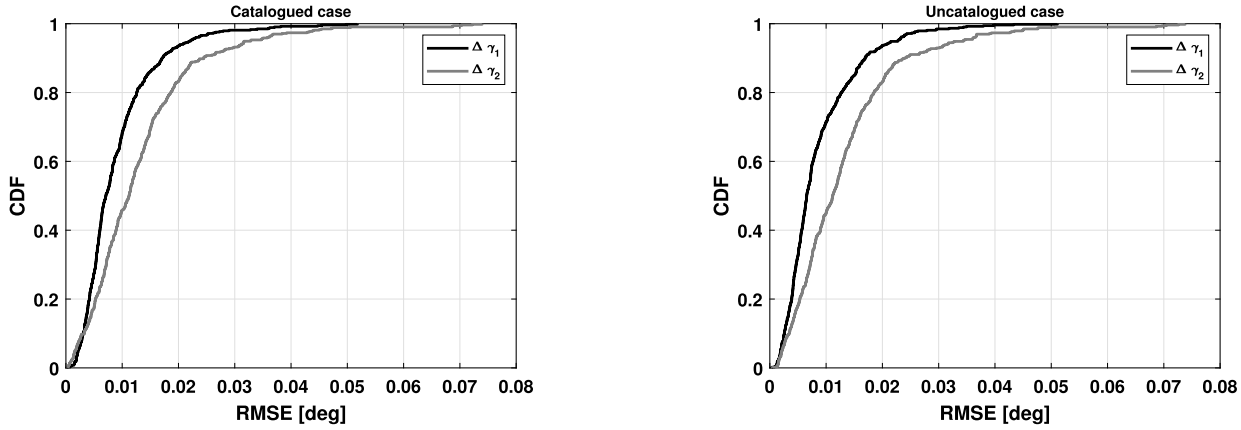

(a) Catalogued case. (b) Uncatalogued case.

Fig. 7. Survey nominal simulation: CDF of the angular RMSE for the catalogued case.

Table 3
Survey nominal simulation: statistical analysis on synthetic data, for catalogued and uncatalogued case.

	25%	50%	75%
Catalogued			
$\eta_{\Delta\gamma_1}$ [deg]	4.7e-03	7.1e-03	1.1e-02
$\eta_{\Delta\gamma_2}$ [deg]	6.4e-03	1.1e-02	1.7e-02
Uncatalogued			
$\eta_{\Delta\gamma_1}$ [deg]	4.2e-03	6.6e-03	1.1e-02
$\eta_{\Delta\gamma_2}$ [deg]	6.5e-03	1.1e-02	1.7e-02

1e-02 deg, and this confirms the accurate performance of MATER in reconstructing the angular track for a set of catalogued objects simultaneously detected. Then, it is worth observing that, for all the quartiles, the angular RMSE is lower in the E-W direction ($\eta_{\Delta\gamma_1}$) than in the N-S one ($\eta_{\Delta\gamma_2}$), although the latter is expected to feature a higher resolution, as discussed in Sec. 5.1. This is due to the length of the angular path travelled during the integration time, as the estimated DOA may correspond to any actual value assumed in the meanwhile. Since most of the data set transits correspond to high-inclination orbits (both prograde and retrograde), the angular path travelled in the N-S direction is usually larger than the one travelled in the E-W one, and this makes the median angular RMSE larger along $\Delta\gamma_2$ than along $\Delta\gamma_1$. All these considerations are valid also for the Cumulative Distribution Function (CDF) plot of the angular RMSE, which is represented in Fig. 7a. In particular, it is possible to observe that, at a given occurrence, the $\Delta\gamma_1$ trend is always at the left of the $\Delta\gamma_2$ one, as it presents a lower angular RMSE, but in the bottom left of the graph. Indeed, there is a portion of data set passes for which the RMSE is dominated by the sensor resolution (finer along $\Delta\gamma_2$ than along $\Delta\gamma_1$).

A detailed computational demand analysis is beyond the purpose of this work, given the current prototype implementation in MATLAB [24], but it can be quantified in less than 10 s per track by using a single core with an Intel(R) Core(TM) i7-8700 CPU @ 3.20 GHz - 3.19 GHz processor. It is worth to point out that the computational time is proportional to the observation time length and the number of sources detected.

Then, MATER is applied on the same transits in the uncatalogued case, that is by considering no a-priori orbital estimate for the observed objects, and solving the ambiguity according to the *delta-k* method. The results are still reported in Table 3 and show that the accuracy is similar to the catalogued case one. As above, Fig. 7b reports the CDF for the uncatalogued case, with similar considerations as for the catalogued one.

Under the same conditions, the computational demand increases with respect to the catalogued case for two reasons. First, the angular track estimation evaluates Eq. (9) on a discrete grid to retrieve the optimisation first guesses, and the finer the grid the more the computations are reiterated. Then, this process is repeated for two CMs sequence in a parallel way, and this almost double the overall computational time. As in the catalogued case, the single slot computational demand also depends on the observation time length and the number of sources detected.

5.3. Sensitivity analysis

The DOA estimation accuracy depends on the SNR level detected, which is strongly linked to the received power P_{rx} and, so, to all the quantities involved in Eq. (14). Hence, a modification of these parameters would affect MATER performance, as the DOA estimation would result noisier. On the one hand, this would provoke a deterioration of the angular track accuracy. On the other hand, the correct DOA estimation could vary more than the angular shift induced by the frequency difference, thus affecting the *delta-k* method robustness in the uncatalogued case. In addition, a reduction in the transmitted power shortens the length of the detected signal, as in FoV side regions the signal would be too weak to be detected.

To better analyse the performance deterioration, a sensitivity analysis is carried out as in [16] on the uncatalogued case, considering lower transmitted power P_{tx} levels: 1e+04 W, 5e+03 W, and 1e+03 W. Besides reproducing a generic loss, a transmitted power decrease can occur operationally for a reduction in the transmitting station electric feed. The shortening of the detected signal length decreases the number of temporally overlapping transits, as represented in Table 4, and no temporally overlapping sources are present for the 1e+03 W transmitted power case. Therefore, a decrease of the transmitted power makes the detected tracks less overlapping, such that they are analysed separately. This may imply an advantage in terms of algorithm complexity, but the portion of the detected tracks becomes shorter and shorter, and this is eventually a drawback in terms of orbit determination routines and of contribution to catalogue maintenance.

The analysis results are reported in Table 5, but for the 1e+03 W transmitted power case, as it does not present any multiple sources detection. It can be noticed that the transmitted power reduction increases the angular RMSE, but the deterioration is not remarkable. Indeed, for the detected portion of the track, the signal is sufficiently effective to prevent from a particularly noisier estimation. Thus, the actual deterioration is represented by the detection length rather than the angular accuracy.

Table 4
Survey sensitivity simulation: slots composed of passes temporally overlapping each other, by varying the transmitted power.

N. of passes per slot	TX Power [W]	2	3	4	5	6	7	8	TOT
Obj. per slot	1e+04	90	14	4	2	1	0	0	254
	5e+03	57	8	3	1	0	0	0	155
	1e+03	0	0	0	0	0	0	0	0

Table 5
Survey sensitivity simulation: statistical analysis on synthetic data, for the uncatalogued case, by varying the transmitted power.

	25%	50%	75%
$P_{tx} = 1e+04$ W			
$\eta_{\Delta\gamma_1}$ [deg]	5.2e-03	7.8e-03	1.2e-02
$\eta_{\Delta\gamma_2}$ [deg]	7.4e-03	1.2e-02	1.7e-02
$P_{tx} = 5e+03$ W			
$\eta_{\Delta\gamma_1}$ [deg]	5.8e-03	9.2e-03	1.4e-03
$\eta_{\Delta\gamma_2}$ [deg]	7.8e-03	1.2e-02	1.7e-02

6. Close proximity operation

As mentioned in Sec. 1, a channelisation strategy can be designed which, focusing on the frequencies of a detected source, filters out the rest of the receiver bandwidth. On the one hand, this operation reduces the Bw term in Eq. (13) and, so, increases the SNR, resulting in a more accurate DOA estimation. On the other hand, it rejects the signal emitted by other sources, and this, in survey observations, reduces the multiple sources scenario to a single source one. This is not the case when the detected sources feature a similar relative velocity with respect to the sensor stations and, so, a similar Doppler shift effect of the signal radiated by the transmitter, that is similar frequencies. In SST-related activities this situation typically occurs in close proximity operations monitoring and fragments cloud observations. Thus, these two scenarios are analysed through numerical simulations.

The first analysis regards the proximity operation [9]. These scenarios are of increasing concern, given the importance attributed to the satellite inspections activities, both for military and civilian applications. An example of the latter application are the operations studied for the active debris removal programs and in orbit self assembly [7].

In this simulation, the proximity operation is represented by a chaser moving around the target according to the safety ellipse model [25], for which the period of the relative orbit is equivalent to the target orbit one. In such a model, the relative orbit semi-major axis is aligned towards the transversal direction of the target Radial-Transversal-Normal (RTN) reference frame [26], and it is doubled with respect to the semi-minor axis. In the analysed scenario, the relative orbit semi-major and semi-minor axes are set equal to 10 km and 5 km respectively, the latter being aligned towards the radial direction (no cross-track component is considered). Fig. 8a shows the selected relative orbit in the target RTN reference frame.

The observation geometry used in the simulation is retrieved from the ISS transit prediction on April 28th, 2021. The trajectory is propagated through SGP4 [23], and the ISS orbital parameters are reported in Table 6, except the true anomaly (as it changes during the transit). BIRALES receiver pointing is kept southwards at an elevation of 83.9 deg, whereas the transmitter pointing angles are 19.3 deg in azimuth and 35.1 deg in elevation. The ISS ephemeris is used to retrieve the target orbital state (its RCS is set equal to 1 m^2), and the chaser relative orbit is generated around it. Four cases are assessed, in terms of angular distance of the chaser in the transversal-radial reference frame, at the initial observation epoch, moving in clockwise direction from the point placed at 10 km and 0 km from the target, along radial and transversal direction respectively: 0 deg (positive transversal distance), 90 deg (negative radial distance), 180 deg (negative transversal distance), 270 deg (positive radial distance). These four cases are represented in Fig. 8b. It is important to point out that, being the observation time window about 3 order of magnitude smaller than the target orbital period (and, so, of the relative orbit period as well), the angular position of the chaser with respect to the target does not change significantly from the initial conditions during the observation.

Table 6
Proximity operation simulation: International Space Station orbital parameters, in terms of semi-major axis (a), eccentricity (e), inclination (i), right ascension of the ascending node (Ω) and argument of periapsis (ω).

a [km]	e	i [deg]	Ω [deg]	ω [deg]
6794.9	6.1e-04	51.5	228.8	45.6

Table 7
Proximity operation simulation: angular root mean square difference (RMSD) in the receiver FoV.

	$\text{RMSD}_{\Delta\gamma_1}$ [deg]	$\text{RMSD}_{\Delta\gamma_2}$ [deg]
0 deg	1.4e+00	7.70e-01
90 deg	3.5e-02	1.1e-01
180 deg	1.4e+00	7.8e-01
270 deg	3.4e-02	1.01e-01

The chaser position in the relative orbit has an impact on the mutual positions between target and chaser angular tracks in the receiver FoV, as clearly visible in Fig. 9a and Fig. 9b. In particular, those situations for which the distance chaser-target is along the target transversal direction (0 deg and 180 deg) feature almost aligned tracks in the FoV, but with a time gap, as the chaser is either in advance (0 deg situation) or in late (180 deg). This motivates, in the track refinement phase, a cluster performed on time coordinates. On the contrary, the situations for which the distance chaser-target is along the radial direction (90 deg and 270 deg) feature parallel tracks in the FoV. Therefore, this motivates the choice of clustering in the FoV, as described in Sec. 4.

The angular difference between the sources in the receiver FoV is reported in Table 7 in terms of Root Mean Square Difference (RMSD) between the predicted tracks. It is possible to notice that the transversal separation (cases 0 deg and 180 deg) causes remarkable angular differences, while the radial one does not (cases 90 deg and 270 deg). Besides their magnitude (10 km and 5 km respectively), this is mainly due to the fact that the line receiver-target is almost aligned towards the target radial direction, considering that the sensor pointing is close to the zenith (83.9 deg). So, a radial separation of the chaser makes it either almost hiding or almost being hidden by the target, and, so, the two sources result extremely close in the receiver FoV on both $\Delta\gamma_1$ and $\Delta\gamma_2$. On the contrary, the separation in transversal direction introduces a time difference between target and chaser, which results in a larger separation in the receiver FoV between the two sources, moreover along $\Delta\gamma_1$, as they move along that direction more.

For each case, MATER is run on simulated data considering three different scenarios: the catalogued, the uncatalogued and the semi-uncatalogued one. In this last situation, one of the two observed objects (in this case the target) is considered as catalogued, while the latter is not, and this allows to have, at the end of the track estimate phase, a FoV less populated of DOAs estimations, as the target ambiguities have been already solved. Fig. 10 shows the result difference, at the end of the track estimate phase, between the uncatalogued (Fig. 10a) and the semi-uncatalogued (Fig. 10b) scenarios (for the 0 deg case), for the two

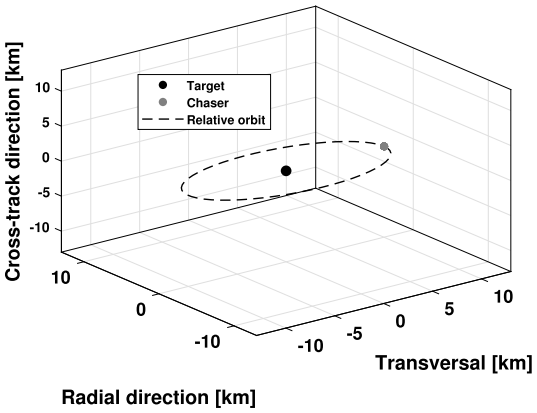

(a) RTN reference frame.

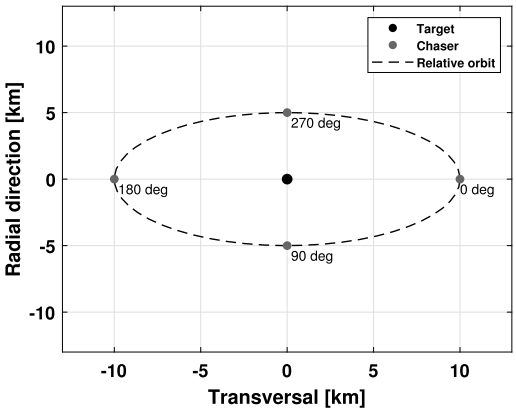

(b) TR reference frame.

Fig. 8. Proximity operation simulation: relative orbit according to the safety ellipse model. In Fig. 8b the four analysed chaser angular positions with respect to the target are represented as well.

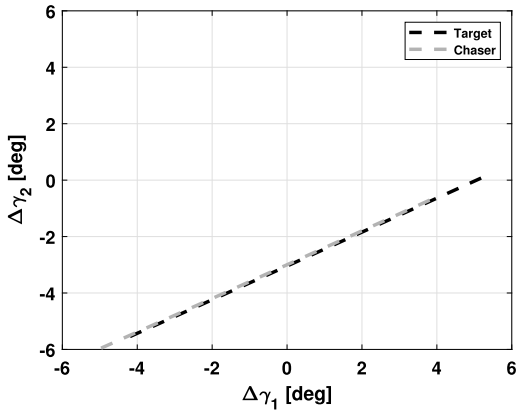

(a) 0 deg situation.

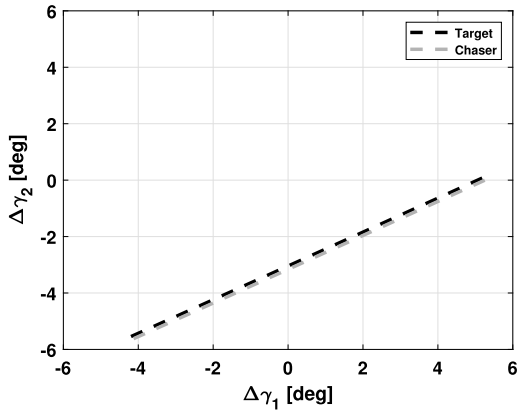

(b) 90 deg situation.

Fig. 9. Proximity operation simulation: predicted angular track in the receiver FoV.

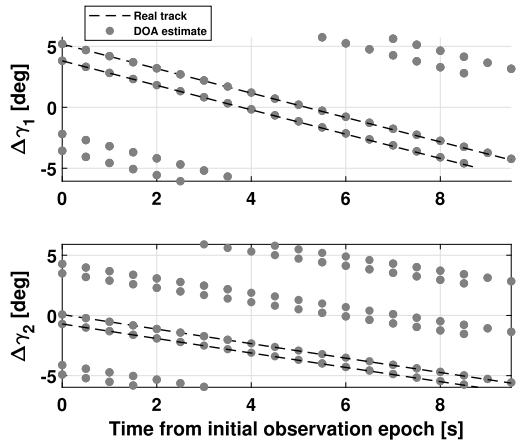

(a) Uncatalogued scenario.

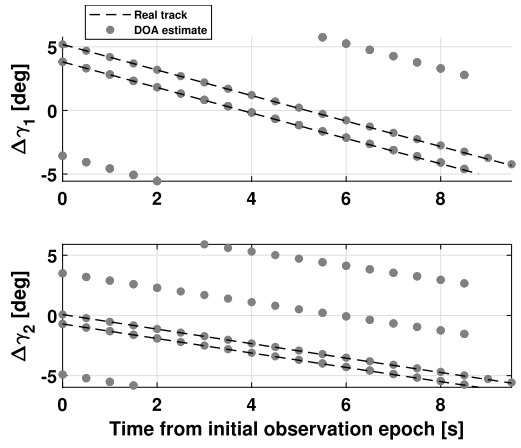

(b) Semi-uncatalogued scenario.

Fig. 10. Proximity operation simulation: track estimate phase result, represented through the two angular coordinates trends in time.

angular coordinates separately: in the former all the DOAs are kept, both for the target and the chaser, while in the latter just the chaser ambiguities remain, as the target ones have been removed.

Table 8 shows the results of the analysis, in terms of success rate in solving the angular track ("Convergence" column) and angular RMSE, for the target and the chaser. It can be seen that the angular accuracy deteriorates with respect to the nominal analysis in Sec. 5, and this is basically due to the mutual interference produced by the two sources, which are close each other for the entire observation and whose frequencies are similar. Overall, it can be noticed that the $\Delta\gamma_1$ RMSE is

Table 8
Proximity operation simulation: results.

	Convergence	$RMSE^{t}_{\Delta\gamma_1}$ [deg]	$RMSE^{t}_{\Delta\gamma_2}$ [deg]	$RMSE^{ch}_{\Delta\gamma_1}$ [deg]	$RMSE^{ch}_{\Delta\gamma_2}$ [deg]
0 deg					
Catalogued	yes	5.6e-02	3.4e-02	5.2e-02	2.9e-02
Uncatalogued	yes	5.6e-02	3.4e-02	5.2e-02	3.1e-02
Semi-uncatalogued	yes	5.8e-02	3.4e-02	5.3e-02	3.1e-02
90 deg					
Catalogued	no	6.3e-02	3.5e-02	7.1e-02	1.3e-01
Uncatalogued	no	5.2e-02	4.4e-02	5.6e-02	5.6e-02
Semi-uncatalogued	no	5.8e-02	3.4e-02	6.6e-02	1.1e-01
180 deg					
Catalogued	yes	5.6e-02	3.5e-02	5.8e-02	3.4e-02
Uncatalogued	yes	5.6e-02	3.4e-02	5.8e-02	3.5e-02
Semi-uncatalogued	yes	5.8e-02	3.4e-02	5.8e-02	3.5e-02
270 deg					
Catalogued	no	7.1e-02	1.3e-01	6.2e-02	3.5e-02
Uncatalogued	no	5.2e-02	4.8e-02	5.0e-02	5.9e-02
Semi-uncatalogued	no	5.8e-02	3.4e-02	6.0e-02	4.0e-02

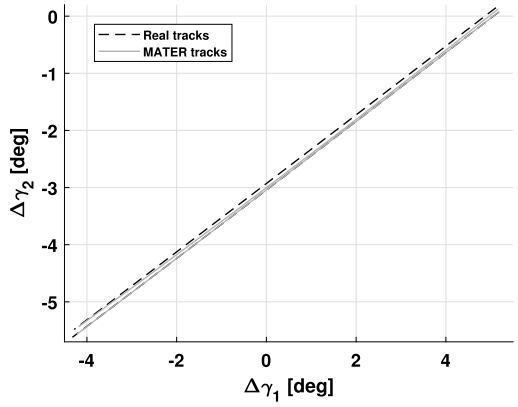

Fig. 11. Proximity operation simulation: MATER failure for the scenario semi-uncatalogued 270 deg. It can be seen that the tracks are erroneously estimated, even if the angular RMSE is low.

slightly larger than the $\Delta\gamma_2$ one, that is the contrary of simulations in Sec. 5. Indeed, the angular paths covered by the source along the two angular directions are similar, given the 51.5 deg inclination of the ISS (Table 6). In particular, as mentioned above, the sources move along $\Delta\gamma_1$ direction a bit more, and this, coupled with the theoretical angular accuracy relationship discussed in Sec. 5.1, makes the estimation along $\Delta\gamma_2$ finer than along $\Delta\gamma_1$.

Both for the catalogued, uncatalogued and semi-uncatalogued scenario, the 0 deg and the 180 deg cases converge to the correct solution, while the others do not, even if they always exhibit a similar angular accuracy. Indeed, comparing the results in Table 8 with the values in Table 7, it can be observed that the angular accuracy is much smaller than the predicted angular distance in the 0 deg and 180 deg cases, while it is of comparable magnitude in the 90 deg and 270 deg ones. In this two latter situations, the sources are so close each other that, also because of the noise, the clustering phase possibly erroneously group the signal DOAs, gathering estimations related to different sources in a same cluster. This results in erroneous tracks, as represented in Fig. 11, which shows a zoomed FoV to better appreciate the failure.

Regardless the track reconstruction accuracy, the presence of two targets can be assessed by looking at the CM eigenvalues trends, as shown in Fig. 12. It is always possible to identify 2 sources, that is 2 eigenvalues trends which are remarkably different from the noise ones (slightly visible in the bottom of the graph). However this is better visible in the 0 deg and 180 deg configurations (Fig. 12a and Fig. 12c), whereas in the 90 deg and 270 deg configurations (Fig. 12b and Fig. 12d) the first eigenvalue increases in magnitude and the second one decreases with respect to the other two cases. Another aspect to point out is that, in the 0 deg graph (Fig. 12a), 2 sources are visible from the beginning, and in the very final instants of the observation time just one remains, while the situation is opposite in the 180 deg graph (Fig. 12c). This is due to the fact that the observation, and so the time window of the measurements acquisition, is planned based on the target visibility. Indeed, in the 0 deg configuration (Fig. 12a), the chaser is already present in the receiver FoV when the target is first detected, as it moves in advance, and 2 sources are present. Then, in the final instants of the target object visibility, the chaser is not in the FoV anymore, and so only 1 source is present. The situation is opposite in the 180 deg configuration (Fig. 12c).

Table 9
Fragments cloud simulation: distribution of the fragments orbital characteristics, in terms of the three quartiles of semi-major axis (a), eccentricity (e), inclination (i), right ascension of the ascending node (Ω) and argument of periapsis (ω).

	a [km]	e	i [deg]	Ω [deg]	ω [deg]
25%	6784.7	2.0e-03	51.5	228.7	127.4
50%	6798.7	3.4e-03	51.6	228.8	206.8
75%	6816.9	5.0e-03	51.6	228.9	322.2

7. Fragments cloud observation

Generally speaking, a fragmentation event can be originated either by a single spacecraft explosion or a collision between two satellites [27]. The widely used NASA Standard Break-up model [28] provides a distribution of fragmentation impulses and physical characteristics of the cloud which depends on the involved satellite characteristics.

The NASA Standard Break-up Model is here applied to create a fragments cloud which is then observed by BIRALES. Analogously to the simulation in Sec. 6, the ISS transit prediction is here considered as the parent object ephemeris. The fragmentation event is set to 08:00:00 (UTC), and Table 9 shows the distribution of the target orbital characteristics, in terms of quartiles on semi-major axis, eccentricity, inclination, right ascension of the ascending node, and argument of periapsis. The generated fragments are propagated and MATER is applied to those detected by BIRALES sensor. To assess the algorithm sensitivity on fragment size, an analysis is carried out considering different RCS: 1 m^2, 0.1 m^2, 0.01 m^2.

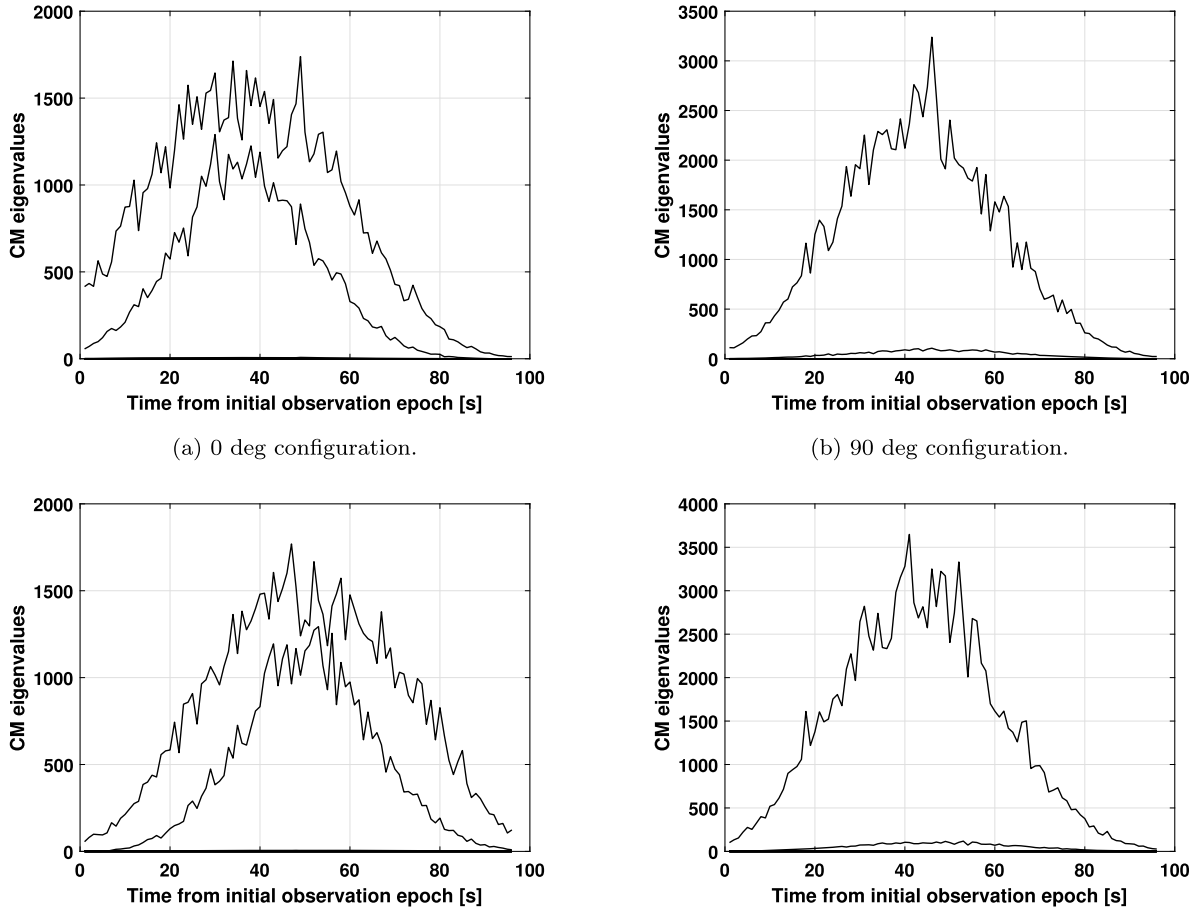

(a) 0 deg configuration.

(b) 90 deg configuration.

(c) 180 deg configuration.

(d) 270 deg configuration.

Fig. 12. Proximity operation simulation: CM eigenvalues trend for the four configurations. It is possible to notice that two trends are always present, but they are better visible in the 0 deg and in the 180 deg configurations.

Table 10
Fragments cloud simulation: slots composed of fragments temporally superimposing each other, by varying the fragment RCS.

N. of passes per slot	RCS [m^2]	2	3	4	5	6	7	8	9	TOT
Obj. per slot	1	21	11	4	0	1	0	0	1	102
	0.1	21	9	3	1	1	0	0	1	100
	0.01	23	8	1	0	1	0	0	0	80

Table 11
Fragments cloud simulation: statistical analysis on fragmentation scenario, by varying the detected fragment RCS.

	25%	50%	75%
1 m2			
$\eta_{\Delta\gamma_1}$ [deg]	2.9e-02	4.5e-02	5.6e-02
$\eta_{\Delta\gamma_2}$ [deg]	1.8e-02	2.7e-02	3.5e-02
0.1 m2			
$\eta_{\Delta\gamma_1}$ [deg]	3.0e-02	4.6e-02	5.6e-02
$\eta_{\Delta\gamma_2}$ [deg]	1.8e-02	2.9e-02	3.5e-02
0.01 m2			
$\eta_{\Delta\gamma_1}$ [deg]	3.0e-03	4.7e-03	5.7e-02
$\eta_{\Delta\gamma_2}$ [deg]	1.9e-03	2.9e-02	3.6e-02

For them, Table 10 reports the correspondence between the number of overlapping transits and slots, and the total number of observed fragments. It is possible to notice that the smaller the RCS, the less the observed objects and the less overlapping the transits are, as a smaller portion of each pass is detected, similarly to the sensitivity analysis considerations in Sec. 5.3.

Table 11 shows the MATER results for the analysis, where it is possible to see that the angular accuracy along $\Delta\gamma_2$ is a little finer than along $\Delta\gamma_1$. This is due both to the angular path travelled and to the sensor resolution, as discussed in Sec. 6. The accuracy slightly deteriorates with the RCS decrease and, overall, some failures occur. In particular, in the 1 m^2 case MATER does not reconstruct the track of one object: it is a fragment marginally illuminated by the TRF (its projected track crosses a side region of the transmitter FoV) and its SNR is so small that, although detected, it is completely hidden by the other sources, as represented in Fig. 13a. This, in the track estimate phase, makes the pattern associated to the weakest source very noisy along all its detection, and the associated maximisation of Eq. (9) converge to noise values. For this reason, no DOA estimation of that source is present at the end of the track estimate phase, as can be seen in Fig. 13b, and this provokes the failure of MATER for this source observation. In the 0.1 m^2 case, this fragment is not detected anymore, but another failure occurs involving two fragments whose actual tracks are so close in the receiver

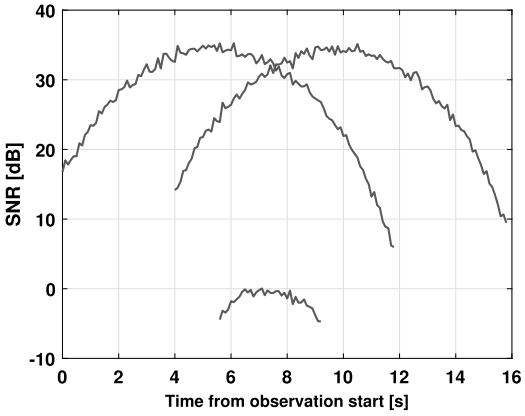

(a) SNR trends.

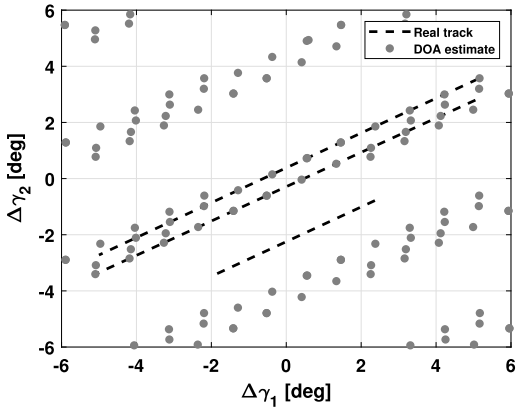

(b) DOA estimations.

Fig. 13. Fragments cloud simulation: MATER failure case in the analysis which considers 1 m^2 RCS for all the fragments. It is possible to notice that the smallest SNR is completely hidden by the other two (in Fig. 13a) and that no DOA estimation related to the shortest track is present, as it is related to the weakest source detected (in Fig. 13b).

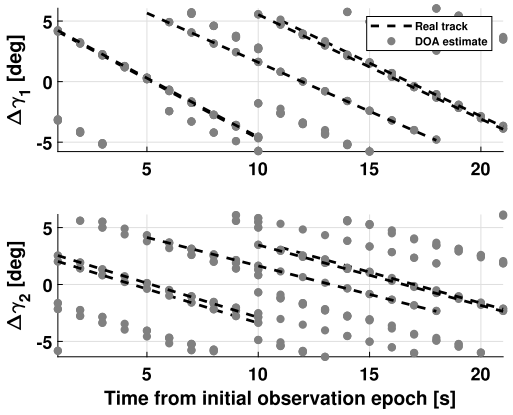

Fig. 14. Fragments cloud simulation: DOA estimation of the failure case in the analysis which considers 0.1 m^2 RCS for all the fragments. It is possible to notice that the last two detected sources are so close that cannot be distinguished in the clustering phase.

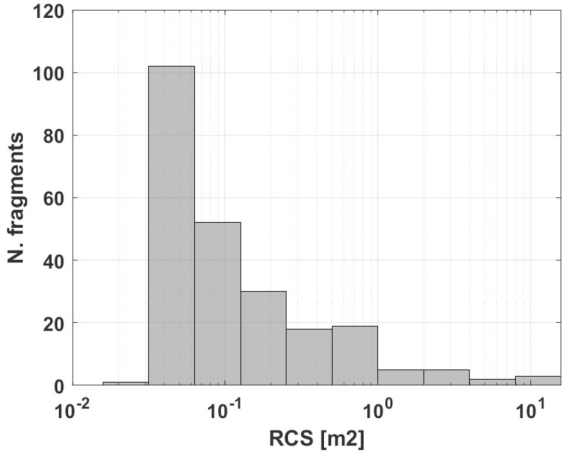

Fig. 15. Fragments cloud simulation: logarithmic distribution of the detected target RCS, which are assumed equal to the fragments cross section modelled according to the NASA Standard Break-up model.

FoV that they cannot be separately estimated. Fig. 14 reports the DOA estimation in time for the two angular coordinates separately. The two failures regard the last two fragments detected, whose estimated DOAs cannot be distinguished during the clustering phase. This issue does not occur in the 1 m^2 scenario, because of the larger SNR, which makes the DOA estimations less noisy for both of the sources and allows the clustering to distinguish them. In the 0.01 m^2 case these fragments are not detected anymore, and no failure occurs.

To conclude, the same analysis is carried out by using the fragment cross section derived from the NASA Standard Break-up Model as target RCS, and considering also the single source transit, that is like in a realistic fragments cloud observation. The RCS logarithmic distribution is reported in Fig. 15, where it can be appreciated that the vast majority of the targets have a RCS much smaller than 1 m^2. The correspondence between the number of intersecting transits and slots is reported in Table 12, and the results are shown in Table 13. It can be noticed that they are similar to the ones in Table 11, and similar considerations apply.

Table 12
Fragments cloud simulation: slots composed of fragments temporally overlapping each other, considering the NASA Standard Break-up Model fragment cross section as RCS. Also the single source cases are considered.

N. of passes per slot	1	2	3	4	5	6	7	8	9	TOT
Obj. per slot	88	20	9	3	0	1	0	0	1	182

Table 13
Fragments cloud simulation: fragmentation scenario, considering the NASA Standard Break-up Model fragment cross section as RCS. Also single transits are considered.

	25%	50%	75%
$\eta_{\Delta\gamma_1}$ [deg]	3.8e-02	4.7e-02	5.8e-02
$\eta_{\Delta\gamma_2}$ [deg]	2.3e-02	2.9e-02	3.5e-02

8. Conclusions

This work presented the MATER algorithm extension to retrieve the angular track measurements when multiple sources are simultaneously detected by a survey radar equipped with an array receiver. The numerical analysis proved the algorithm potential in survey observations, and the detection length depends on the impinging signal intensity, which in turns depends on many factors such as the transmitted power. In SST-related activities this MATER extension can be applied in particular during observations of a proximity operation and of a fragments cloud. Concerning the former, the presence of the two sources can be confirmed by analysing the CM eigenvalues, and the angular track ac-

curacy depends on the mutual alignment between target and chaser. Regarding the fragments cloud observation, both the accuracy and the resolution depend moreover on the size of the observed fragment.

Future works will focus on a signal channelisation strategy which allows to maximise the detected SNR, with benefit both for angular track accuracy and length. Based on this, an extensive validation campaign on real data will be conducted to make MATER operational.

CRediT authorship contribution statement

M.F. Montaruli: Conceptualization, Data curation, Formal analysis, Investigation, Methodology, Software, Validation, Visualization, Writing – original draft, Writing – review & editing. **P. Di Lizia:** Conceptualization, Formal analysis, Investigation, Supervision, Writing – review & editing, Methodology. **S. Tebaldini:** Methodology, Supervision, Writing – review & editing, Formal analysis. **G. Bianchi:** Funding acquisition, Project administration, Resources, Writing – review & editing.

Declaration of competing interest

The authors declare that they have no conflict of interest.

Data availability

The data that has been used is confidential.

Acknowledgements

The research activities described in this paper were carried out with the contribution of the NextGenerationEU funds within the National Recovery and Resilience Plan (PNRR), Mission 4—Education and Research, Component 2— From Research to Business (M4C2), Investment Line 3.1—Strengthening and creation of Research Infrastructures, Project IR0000026 - Next Generation Croce del Nord - Project Identification Code (CUP) C53C22000880006.

References

[1] M.-H. Lee, C.-O. Min, Y.-S. Kim, D.-W. Lee, K.-R. Cho, Analysis of population damage by space debris upon collision with Earth based on the reverse geocoding method, Aerosp. Sci. Technol. 50 (2016) 139–148, https://doi.org/10.1016/j.ast.2015.12.030, https://www.sciencedirect.com/science/article/pii/S1270963815300328.

[2] S. Bonaccorsi, M.F. Montaruli, P. Di Lizia, M. Peroni, A. Panico, M. Rigamonti, F. Del Prete, Conjunction analysis software suite for space surveillance and tracking, Aerospace 11 (2) (2024), https://doi.org/10.3390/aerospace11020122, https://www.mdpi.com/2226-4310/11/2/122.

[3] K. Lee, C. Park, S.-Y. Park, Near-optimal continuous control for spacecraft collision avoidance maneuvers via generating functions, Aerosp. Sci. Technol. 62 (2017) 65–74, https://doi.org/10.1016/j.ast.2016.11.026, https://www.sciencedirect.com/science/article/pii/S127096381630339X.

[4] F. Sanson, C. Bertorello, J.-M. Bouilly, P.M. Congedo, Breakup prediction under uncertainty: application to upper stage controlled reentries from GTO orbit, Aerosp. Sci. Technol. 87 (2019) 340–356, https://doi.org/10.1016/j.ast.2019.02.031, https://www.sciencedirect.com/science/article/pii/S127096381831719X.

[5] M.F. Montaruli, P.D. Lizia, E. Cordelli, H. Ma, J. Siminski, A stochastic approach to detect fragmentation epoch from a single fragment orbit determination, Adv. Space Res. (2023), https://doi.org/10.1016/j.asr.2023.08.031, https://www.sciencedirect.com/science/article/pii/S0273117723006798.

[6] A. Pastor, G. Escribano, M. Sanjurjo-Rivo, D. Escobar, Satellite maneuver detection and estimation with optical survey observations, J. Astronaut. Sci. 69 (3) (2022) 879–917, https://doi.org/10.1007/s40295-022-00311-5, https://www.scopus.com/inward/record.uri?eid=2-s2.0-85131520993&doi=10.1007%2fs40295-022-00311-5&partnerID=40&md5=c3cc1c7a6ef0c5cecc1f7734328dc9d3.

[7] M. Okasha, C. Park, S.-Y. Park, Guidance and control for satellite in-orbit-self-assembly proximity operations, Aerosp. Sci. Technol. 41 (2015) 289–302, https://doi.org/10.1016/j.ast.2014.11.011, https://www.sciencedirect.com/science/article/pii/S1270963814002569.

[8] V. Pesce, R. Opromolla, S. Sarno, M. Lavagna, M. Grassi, Autonomous relative navigation around uncooperative spacecraft based on a single camera, Aerosp. Sci. Technol. 84 (2019) 1070–1080, https://doi.org/10.1016/j.ast.2018.11.042, https://www.sciencedirect.com/science/article/pii/S1270963818317346.

[9] M. Maestrini, M.A. De Luca, P. Di Lizia, Relative navigation strategy about unknown and uncooperative targets, J. Guid. Control Dyn. 46 (9) (2023) 1708–1725, https://doi.org/10.2514/1.G007337, https://doi.org/10.2514/1.G007337.

[10] M.F. Montaruli, G. Purpura, R. Cipollone, A. De Vittori, L. Facchini, P. Di Lizia, M. Massari, M. Peroni, A. Panico, A. Cecchini, M. Rigamonti, An orbit determination software suite for space surveillance and tracking applications, CEAS Space J. (2024), https://doi.org/10.1007/s12567-024-00535-1.

[11] H. Wilden, B.N. Bekhti, R. Hoffmann, C. Kirchner, R. Kohlleppel, C. Reising, A. Brenner, T. Eversberg, GESTRA - recent progress, mode design and signal processing, in: 2019 IEEE International Symposium on Phased Array System Technology (PAST), 2019, pp. 1–8, 10.1109/PAST43306.2019.9020744.

[12] R.C. Gómez, P. Besso, G.M. Pinna, M. Alessandrini, J.M. Salmerón, M.A.R. Prada, Initial operations of the breakthrough Spanish Space Surveillance and Tracking Radar (S3TSR) in the European context, in: 1st NEO and Debris Detection Conference, vol. 1, 2019.

[13] F. Muller, Graves space surveillance system: life extension and upgrade program, in: Proc. 7th European Conference on Space Debris, 2017.

[14] M. Montaruli, L. Facchini, P. Di Lizia, M. Massari, G. Pupillo, G. Bianchi, G. Naldi, Adaptive track estimation on a radar array system for space surveillance, Acta Astronaut. 198 (2022) 111–123, https://doi.org/10.1016/j.actaastro.2022.05.051.

[15] R. Schmidt, Multiple emitter location and signal parameter estimation, IEEE Trans. Antennas Propag. 34 (3) (1986) 276–280, https://doi.org/10.1109/TAP.1986.1143830.

[16] M.F. Montaruli, P. Di Lizia, S. Tebaldini, G. Bianchi, Delta-k approach for space surveillance multireceiver radars, Astrodynamics (2024), https://doi.org/10.1007/s42064-024-0217-5.

[17] H.L. Van Trees, Arrays and spatial filters, in: Optimum Array Processing, John Wiley & Sons, Ltd, 2002, pp. 17–89, Ch. 2.

[18] P. Torr, A. Zisserman, Mlesac: a new robust estimator with application to estimating image geometry, Comput. Vis. Image Underst. 78 (1) (2000) 138–156, https://doi.org/10.1006/cviu.1999.0832, https://www.sciencedirect.com/science/article/pii/S1077314299908329.

[19] G. Bianchi, G. Naldi, F. Fiocchi, P. Di Lizia, C. Bortolotti, A. Mattana, A. Maccaferri, A. Magro, M. Roma, M. Schiaffino, A. Cattani, D. Cutajar, G. Pupillo, F. Perini, L. Facchini, L. Lama, M. Morsiani, M.F. Montaruli, A new concept of bi-static radar for space debris detection and monitoring, https://doi.org/10.1109/ICECCME52200.2021.9590991, https://www.scopus.com/inward/record.uri?eid=2-s2.0-85119418072&doi=10.1109%2fICECCME52200.2021.9590991&partnerID=40&md5=00f78c2fc869199eb6cedf93529a1496, 2021.

[20] R. Peldszus, P. Faucher, European Space Surveillance and Tracking Support Framework, Springer International Publishing, Cham, 2020, pp. 883–904.

[21] G. Bianchi, M.F. Montaruli, M. Roma, S. Mariotti, P. Di Lizia, A. Maccaferri, L. Facchini, C. Bortolotti, R. Minghetti, A new concept of transmitting antenna on bi-static radar for space debris monitoring, https://doi.org/10.1109/ICECCME55909.2022.9988566, https://www.scopus.com/inward/record.uri?eid=2-s2.0-85146427935&doi=10.1109%2fICECCME55909.2022.9988566&partnerID=40&md5=af79351eb347fee90a4a7e4982e465bd, 2022.

[22] M. Losacco, P. Di Lizia, M. Massari, G. Naldi, G. Pupillo, G. Bianchi, J. Siminski, Initial orbit determination with the multibeam radar sensor BIRALES, Acta Astronaut. 167 (2020) 374–390, https://doi.org/10.1016/j.actaastro.2019.10.043, https://www.sciencedirect.com/science/article/pii/S0094576519313712.

[23] D.A. Vallado, P. Crawford, R. Hujsak, T.S. Kelso, Revisiting spacetrack report \#3!, in: AIAA Astrodynamics Specialists Conference and Exhibit, 2006.

[24] MATLAB, The MathWorks Inc., Natick, Massachusetts, 2020, 9.9.0.1538559 (R2020b).

[25] D. Gaylor, B. Barbee, Algorithms for safe spacecraft proximity operations, Adv. Astronaut. Sci. 127 (2007) 133–152.

[26] B.D. Tapley, B.E. Schutz, G.H. Born, Chapter 2 - The orbit problem, in: B.D. Tapley, B.E. Schutz, G.H. Born (Eds.), Statistical Orbit Determination, Academic Press, Burlington, 2004, pp. 17–91, https://www.sciencedirect.com/science/article/pii/B9780126836301500217.

[27] A. Muciaccia, L. Facchini, M.F. Montaruli, G. Purpura, R. Detomaso, C. Colombo, M. Massari, P. Di Lizia, A. Di Cecco, L. Salotti, G. Bianchi, Radar observation and recontruction of cosmos 1408 fragmentation, J. Space Saf. Eng. (2023), https://doi.org/10.1016/j.jsse.2023.11.006, https://www.sciencedirect.com/science/article/pii/S2468896723001131.

[28] N.L. Johnson, P.H. Krisko, J.-C. Lieu, P.D. Anz-Meador, NASA's new breakup model of evolve 4.0, Adv. Space Res. 28 (9) (2001) 1377–1384, https://doi.org/10.1016/S0273-1177(01)00423-9, https://www.sciencedirect.com/science/article/pii/S0273117701004239.